Vapour layer formation by electrical discharges through electrically conducting liquids-modelling and experiment

Schaper, L., Graham, B., & Stalder, K. (2011). Vapour layer formation by electrical discharges through electrically conducting liquids-modelling and experiment. Plasma Sources Science and Technology, 20(3), [034003]. DOI: 10.1088/0963-0252/20/3/034003

Published in:
Plasma Sources Science and Technology

Document Version:
Early version, also known as pre-print

Vapour layer formation by electrical discharges through electrically conducting liquids—modelling and experiment

2011 Plasma Sources Sci. Technol. 20 034003

(http://iopscience.iop.org/0963-0252/20/3/034003)

Plasma Sources Sci. Technol. **20** (2011) 034003 (11pp) doi:10.1088/0963-0252/20/3/034003

Vapour layer formation by electrical discharges through electrically conducting liquids—modelling and experiment

L Schaper, W G Graham and K R Stalder

Centre for Plasma Physics, School of Mathematics and Physics, Queen's University Belfast, Belfast BT7 1NN, UK

E-mail: lschaper01@qub.ac.uk, b.graham@qub.ac.uk and krstalder@staldertechnologies.com

Received 17 August 2010, in final form 29 November 2010
Published 11 April 2011
Online at stacks.iop.org/PSST/20/034003

Abstract

Experimental and finite element modelling methods are used to study the formation of vapour layers in electrical discharges through saline solutions. The experiments utilize shadowgraphic and photometric methods to observe the time dependence of thin vapour layers and plasma formation around electrodes driven by moderate voltage (<500 V) pulses, applied to an electrode immersed in a conducting saline solution. Finite element multiphysics software, coupling thermal and electrical effects, is employed to model the vapour layer formation. All relevant electrical and thermal properties of the saline are incorporated into the model, but hydrodynamic and surface tension effects are ignored. Experimental shadowgraph and modelling images are compared, as are current histories, and the agreement is very good. The comparison of experiment and modelling gives insight into both vapour layer production and subsequent plasma production. We show that, for example, superheating of the saline above its normal vaporization temperature may be playing a significant role in vapour formation. We also show that electric fields of approaching 10^7 V m^{-1} can be achieved in the vapour layer.

(Some figures in this article are in colour only in the electronic version)

1. Introduction

Recently there has been keen interest in the physics and chemistry occurring in electrical discharges through liquids and plasmas formed in these environments. The liquids span many different types, from non-conducting to electrically conducting saline solutions. Much of the interest in discharges in saline solutions is related to biomedical applications, and in particular, plasma-based electrosurgical devices [1]. There are other applications, such as contact glow discharge electrochemical reactors, in which electrical discharges in saline and other fluids produce ionization and chemically active species that can cause modification of surfaces in and around the fluid supporting the discharge [2, 3]. In addition, high-voltage pulsed discharges in low-conductivity water can be used to chemically remediate compounds that are dissolved or suspended in the liquid [4].

Depending on the application, various excitation schemes are used to produce the discharges. Radiofrequency, direct current (dc) and various combinations of these are used to produce the excitation waveform, and these determine some aspects of how the discharges behave. A noteworthy feature of all of these discharges is that, under sufficiently energetic excitation, vapour layers and bubbles are observed. These vapour layers and bubbles are frequently observed near the electrodes that dissipate energy locally at a rate fast enough to exceed the rate at which the energy is conducted or convected away by the liquid, thus raising the local temperatures to above the point at which the fluid vaporizes.

This work seeks, through experiment and finite element multiphysics modelling, to improve our understanding of how vapour layers and plasmas [1] are formed in saline solutions subjected to moderate voltage electrical discharges. It is shown that very large electric fields can develop in thin vapour layers, and these conditions can support the formation of glow discharge plasmas and other types of gas-phase ionization phenomena that have been observed previously [5–7].

2. Experiment

2.1. Experimental apparatus

The experimental apparatus is shown schematically in figure 1. The electrode assembly consists of a vertically mounted

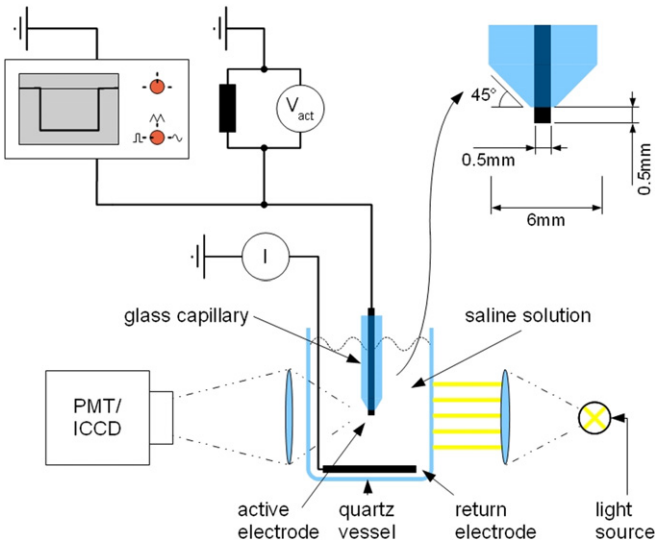

Figure 1. A schematic diagram of the experimental apparatus.

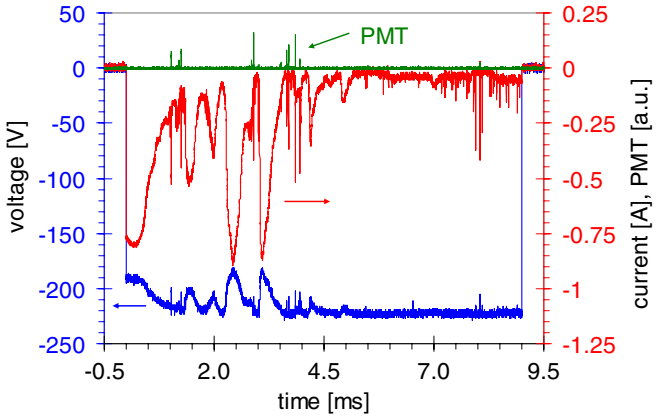

Figure 2. The measured current and voltage time dependence of the system during a 9 ms, −225 V applied voltage pulse with the liquid at room temperature (∼20 °C). Also shown is the response of a fast PMT viewing the electrode tip region.

0.5 mm tungsten rod; the face of the downward facing tip has been ground flat. The electrode is surrounded by a glass capillary, with a conical tip, so that only the bottom 0.5 mm of the tungsten rod is exposed to the liquid. In all the measurements presented here the liquid is a solution of distilled water and 0.9% NaCl. It is contained in a rectangular glass cuvette (60 mm wide, 40 mm long and 60 mm tall). The liquid occupies the first 50 mm of the cuvette, so it has a total volume of 120 mL; the face of the electrode tip is 15 mm below the liquid surface. A grounded titanium return electrode is placed on the bottom of the cuvette at a distance of about 35 mm below the face of the powered electrode. Its exposed area is more than two orders of magnitude larger than the powered electrode so the current density and expected Ohmic heating is much larger at the tungsten electrode than at the grounded electrode. The dependence of the system in response to changes in liquid temperature and voltage pulse amplitude was studied with an emphasis on room temperature and −225 V pulses.

The powered electrode is connected to a pulsed power supply which consists of a fast, negative voltage switch (Behlke HTS 31-06) with 22.4 Ω ballast resistors on the input and output. This can supply a negative dc voltage of up to 500 V with a 20 ns rise time and fall time determined by the *RC* constant of the electric circuit. Voltage pulses of up to 10 ms duration were used with a minimum separation of 0.5 s. The voltage applied to the powered electrode is measured, immediately after the output ballast resistor, using a Tektronix P6015 1000 : 1 voltage probe. The current waveform is obtained with a TCP202 current probe which combines a Hall sensor and coil to measure both the ac and dc components.

Time-resolved changes in the refractive index of the liquid, and hence vapour layer formation, upon the application of the voltage pulse are observed using shadowgraphy. The electrode tip region is backlit by the output of a 60 W halogen lamp which is homogeneously expanded to produce a parallel white light beam. This is in the line of sight of an Andor iStar DH 734 ICCD camera placed behind a quartz glass lens system with ×10 magnification. This produces images with resolution of about 12 μm. The ICCD and a fast photomultiplier tube (PMT) also image and record plasma formation [7].

2.2. *Experimental results*

A typical electrical behaviour of the system is shown in figure 2. Note that the large current draw at early times reduces the −225 V applied voltage to −200 V, hence the latter voltage is used in the simulation of the vapour layer. This electrical behaviour is correlated with the vapour layer development, as is illustrated in figure 3, which is in turn influenced by properties of the liquid and the magnitude of the applied voltage.

Initially the current increases very rapidly. Measurements with higher time resolution (figure 4) show evidence of a sharp peak in the current in the first 5 μs immediately after the voltage is applied and also when it is terminated. While this feature is particularly pronounced at the higher voltages, as in figure 4, it can also be observed with pulses as low as 200 V. We attribute this current increase to the formation and decay of a double layer at the electrode. This is a typical response in any liquid system in which charged particles are present [8]. The charged particles react to inhibit any perturbation caused by applied electric fields and form a space charge layer.

After completion of the double layer formation the current is fairly constant as the vapour layer is formed, but it does always exhibit a slight maximum and starts to decay. When the vapour layer reaches full coverage of the electrode the current rapidly decreases (figure 2). The time to full vapour layer coverage depends on liquid temperature and the magnitude of the applied voltage. For example, at 50 °C and an applied voltage of 225 V full coverage, to a depth of about 25 μm, is achieved after about 0.15 ms (figure 3), whereas at room temperature at the same voltage full coverage is reached after about 0.4 ms and the thickness is about 100 μm. The current continues to decrease for the next 0.25 ms at 50 °C (figure 3) and 0.5 ms at room temperature. During this period the vapour layer reaches a maximum thickness of about 0.25 mm before becoming much less uniform, particularly thinning at the electrode edges (figure 3).

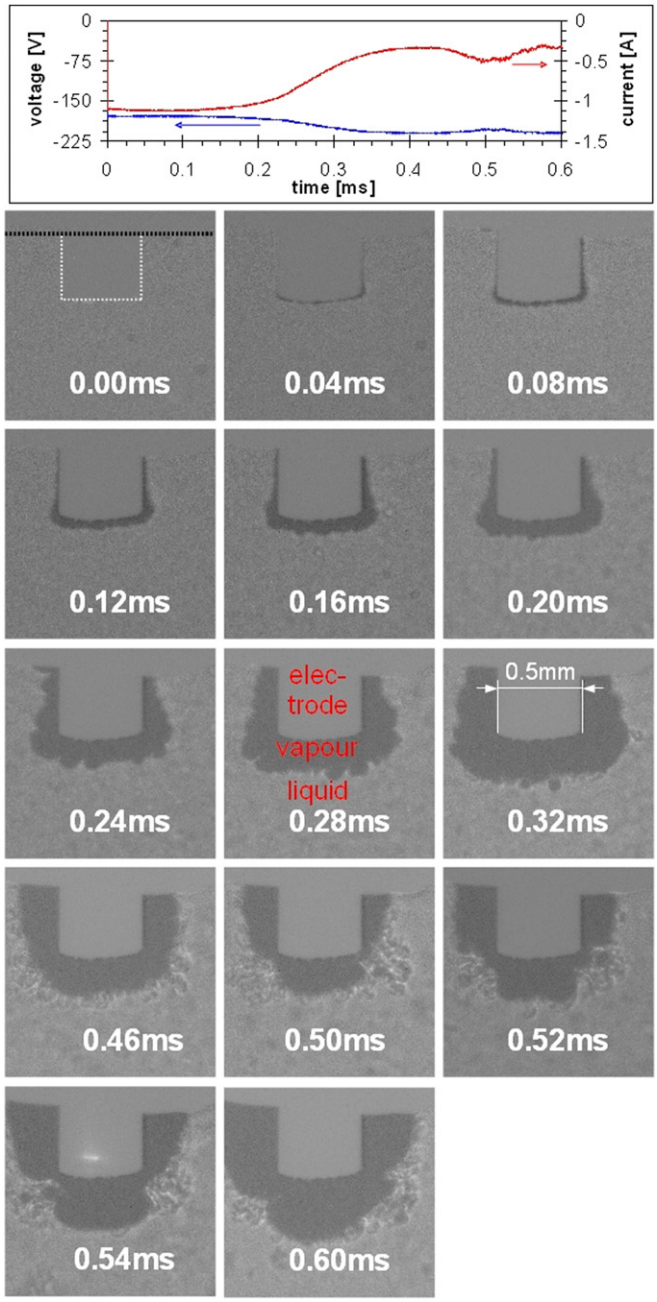

Figure 3. The time dependence of shadowgraphs of the electrode tip area during a series of 9 ms long, −225 V pulses at a liquid temperature of 50 °C. Also shown is the measured current and voltage time dependence.

Under the same experimental conditions this first phase of the electrical behaviour of the system and the vapour layer growth is very reproducible from pulse to pulse and this is the region of primary interest in this paper. Thereafter, as shown in figure 2, the current and vapour layer behaviour are erratic and vary from pulse to pulse. This is a period during which plasmas are formed in the vapour layer [7] (figure 5) as evidenced in the photomultiplier responses seen in figure 2. Also apparent is the circuit impedance, and hence the current, responding to plasma production and the breakup and re-growth of the vapour layer.

After the voltage pulse ends the vapour layer breaks up and bubbles drift into the liquid as shown in figure 6. In about 10% of the pulses the bubbles will adhere to the electrode support or tip and particularly at the glass capillary–tungsten tip interface. Data are only taken after ensuring that no bubbles are present at the start of the voltage pulse. The changing conductivity regimes during the vapour layer formation are reflected in the current–voltage characteristic during that period, as shown in figure 7. This indicates the switch from the double layer formation (0 to 0.5 μs) through the initial Ohmic heating (0.5 to 450 μs) and associated increasing vapour layer coverage of the electrode to the thickening of the vapour layer (450 to 900 μs).

Information about the growth of the vapour layer and its time dependence can be determined from the shadowgraph images. The temporal variation of projected area throughout a voltage pulse is shown in figure 8(a) and the depth of the vapour layer at the tip face in figure 8(b). The conditions are similar to those in figure 2 but each image was recorded during a different pulse. From figures 8(a) and (b) it can be seen that the growth rates are not constant. The initial growth persists for about 450 μs, the time for a complete, uniformly thick vapour layer to form. The bubble-like formations on the surface layer then increase the volume sharply. The vapour layer is then maintained at about the same volume during plasma production and the deformations of the vapour layer. The different symbols are for measurements made on three different days and demonstrate the reproducibility of the vapour layer production ($t \lesssim 0.6$ ms) and the more erratic behaviour of plasma production ($t > 0.6$ ms).

3. Finite element multiphysics model

To better understand some of the physics associated with vapour layer formation, which is a prerequisite for understanding how plasmas are formed, a model employing COMSOL Multiphysics finite element modelling software [9] was developed. Although the phenomena associated with vapour layer formation may be studied through many different coupled multiphysics combinations, the minimum level requires coupling the thermal and electrical physics.

The electrical physics employs Gauss' law and Ohm's law. Ohm's law (equation (2.1)) relates the current density to the electric field strength and Gauss' law (equation (2.2)) is used to solve for the field. The size of the electrodes and the wavelengths associated with the time scales of interest are such that an electrostatic (near field) solution is appropriate. Hence we can relate the electric field through the gradient of the potential V (equation (2.3)). Thus,

$$\vec{J} = \sigma(T)\vec{E} \tag{2.1}$$

$$\nabla \cdot (\varepsilon(T)\vec{E}) = 0 \tag{2.2}$$

$$\vec{E} = -\nabla V, \tag{2.3}$$

where T is the temperature, $\sigma(T)$ is the electrical conductivity, $\varepsilon(T)$ is the dielectric constant, $\vec{J}$ is the current density, $\vec{E}$ is the electric field and V is the scalar electric potential. The

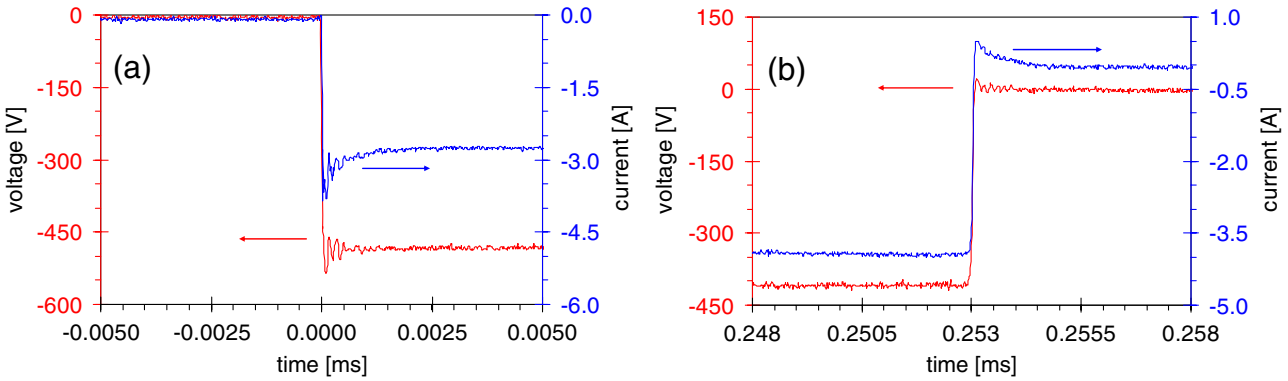

Figure 4. The measured current and voltage time dependence of the system with enhanced time resolution at (*a*) the early and (*b*) the late stage of a 0.25 ms, −500 V pulse at room temperature.

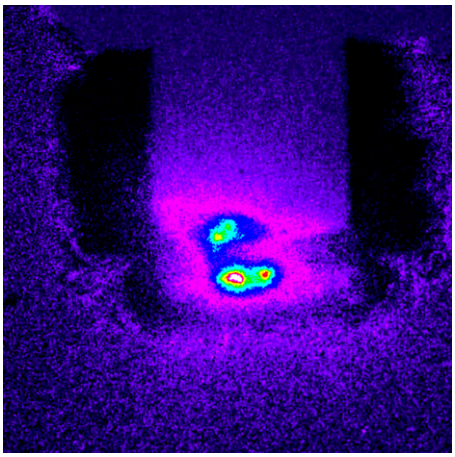

Figure 5. An ICCD image of the first plasma production in a 300 μs, 275 V pulse taken 250 μs after pulse initiation with an exposure time of 10 μs.

appropriate equation system (e.g. SI) must be chosen and used consistently with the dimensions specified in the model. The electrical conductivity and dielectric properties of the materials may be temperature dependent. In particular, the properties of the saline and any vapour layer formed from it are strongly temperature dependent and are responsible for much of the physics we are studying here.

The thermal response is described by the time-dependent heat conduction equation:

$$\rho(T)C_p(T)\frac{\partial T}{\partial t} - \nabla \cdot (k(T)\nabla T) = \vec{J} \cdot \vec{E}, \qquad (2.4)$$

where T is the temperature, t is the time, $\rho(T)$ is the mass density, $C_p(T)$ is the specific heat at constant pressure, $k(T)$ is the thermal conductivity and $\vec{J} \cdot \vec{E}$ is the Ohmic-heating term due to the fields and currents flowing through each region. Note that all of the variables and parameters may vary with the type of material and temperature, as well as position and time. The Ohmic-heating term is most significant in the region containing the saline solution.

In this initial study we used the base COMSOL heat transfer component with temperature T as the dependent variable and coupled that with the generalized electrostatics module with electrical potential V as the dependent variable. The simulations involve numerous steps, including defining the geometry of interest, assigning material properties, assigning boundary conditions, creating a geometrical mesh with sufficient resolution for the problem to be solved, and specifying the numerical solver parameters. Since the phenomena of interest are transient, we solve the problem using a transient solver and plot the solutions at various times. Following successful convergence and completion, the solutions can be post-processed to view many of the parameters of interest.

3.1. Geometrical model

The geometry we modelled was chosen to closely match the experiments conducted in our laboratory as described in section 2. This model was a rather simple cylindrically symmetric (2D-axisymmetric) geometry to simplify both the modelling and comparison with the experiment. The main difference between the model and experiment was the external boundary used to contain the saline: the model uses a 40 mm diameter by 50 mm tall cylinder of similar dimensions to the rectangular cuvette used in the experiments described in section 2. The 2D-axisymmetric model substantially improves numerical convergence and run time. A cross section of the model geometry is shown in figure 9.

3.2. Material constants

Most of the material properties used in the finite element simulations are available in the base Materials Library within COMSOL [9]. The thermal properties of most of the materials (specific heat, thermal conductivity, density, etc) are not temperature dependent. The electrical properties (conductivity, dielectric constant, etc) of most of the materials are also not temperature dependent. However, both the thermal and electrical properties of the saline solution and vapour formed from it (not available in the base Materials Library) are substantially temperature dependent. We detail these properties here.

3.2.1. Saline properties. Saline solutions studied here are derived from aqueous solutions of dissolved salts, and in

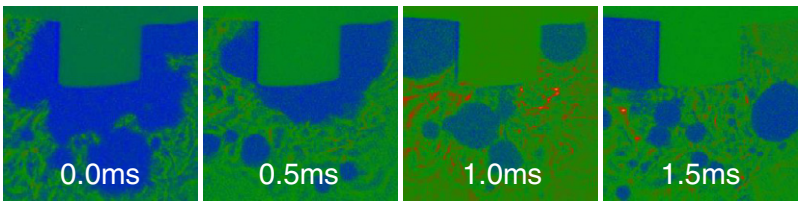

Figure 6. Typical shadowgraphs of the vapour evolution in the electrode tip region following a 4 ms voltage pulse of 225 V at room temperature liquid. Time $t = 0$ indicates the moment when the pulse ends.

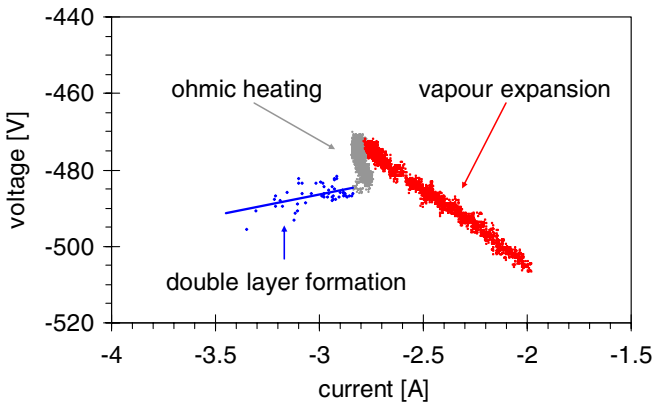

Figure 7. The current–voltage characteristic derived from the current–voltage time dependence for a −500 V pulse at room temperature.

particular sodium chloride (NaCl). Because the vaporizing saline medium undergoes a phase change when its temperature exceeds its boiling point, substantial changes in density, thermal conductivity, and heat capacity, as well as the electrical conductivity occur. Ionic conduction from the dissolved, dissociated, and hydrated salt ions contributes strongly to the electrical conductivity of the saline solution. Moreover, saline solutions typically have a rather substantial temperature coefficient of electrical conductivity, which is related to the temperature coefficient of viscosity of water. Although the model can be used to study almost completely arbitrary saline concentrations, in this work we focus our attention on saline concentrations commonly found in medical situations, namely 0.9% NaCl (0.154 moles litre) by weight in water. We use Stogryn's empirical formula [10] to derive a second-order numerical expression for the electrical conductivity of this liquid saline:

$$\sigma_{\mathrm{L}}(T) = (2.805\text{–}3.887) \times 10^{-2} T + 1.163 \times 10^{-4} T^2,$$

where σ_{L} is the conductivity of liquid saline in $\mathrm{S\,m^{-1}}$, and the temperature T is expressed in K. At 25 °C (293.16 K), $\sigma_{\mathrm{L}} = 1.553\,\mathrm{S\,m^{-1}}$. The boiling point of this saline under typical sea level laboratory pressure conditions (101.325 kPa) is 100.15 °C, slightly larger than 100 °C, due to the presence of ions in solution which attract water molecules and therefore present a barrier to vaporization [11].

Salt ions in aqueous solutions are tightly bound to water molecules. As is well known, under slowly varying conditions, upon vaporization of saline, salt ions do not vaporize. We therefore currently neglect the contribution to vapour phase conductivity from any salt ions that may originate from other non-equilibrium processes, such as sputtering. In this equilibrium model, the electrical conductivity of water vapour does have some contribution due to the ion product of dissociated water ($\mathrm{H_2O} \rightarrow \mathrm{H^+ + OH^-}$) and the hydrated derivatives of these ions. There are scant data regarding the ion composition of water vapour, but there are some data suggesting the equilibrium concentration of ions at near saturation of 100 °C is about $10^7\,\mathrm{cm^{-3}}$, and the mobility of the hydrated ions is about $2\,\mathrm{cm^2\,V^{-1}\,s^{-1}}$ [12]. We thus estimate that the equilibrium conductivity of the water vapour above a saline solution at 100.15 °C is about $\sigma_{\mathrm{V}} = 3.2 \times 10^{-10}\,\mathrm{S\,m^{-1}}$, which is substantially reduced from that of the liquid saline. We retain this small conductivity for the sake of completeness, and it also helps numerical convergence of the stiff differential equations in the computer simulation. Heaviside functions are used to connect the conductivity of the saline and the water vapour as a function of temperature:

$$\sigma(T) = \sigma_{\mathrm{L}}(T)[1 - H(T - T_{\mathrm{vap}})] + \sigma_{\mathrm{V}} H(T - T_{\mathrm{vap}}),$$

where T_{vap} is the vaporization temperature, $H(x) = 1$ for $x > 0$, and $H(x) = 0$ for $x < 0$. In the COMSOL software we use the Heaviside numerical function, flc2hs $(x, 1)$, which is an approximate form of $H(x)$ and has a continuous first and second derivatives, with a unit transition width.

We use similar methodology to compute the other properties of saline and vapour, such as its relative permittivity $\varepsilon(T)$ (liquid [10], vapour [13]), mass density $\rho(T)$ (liquid [14], vapour [15]), specific heat $c(T)$ and [11] thermal conductivity $k(T)$ (liquid [16], vapour [17]). The properties of water vapour are essentially constant over the temperature range of interest for this study so we do not include their weak temperature dependence. We summarize all of the numerical values and formulae used to compute the various physical properties here.

Relative permittivity:

$$\varepsilon(T) = \varepsilon_{\mathrm{L}}(T)[1 - H(T - T_{\mathrm{vap}})] + \varepsilon_{\mathrm{V}} H(T - T_{\mathrm{vap}}),$$

where $\varepsilon_{\mathrm{L}} = 275.52 - 1.0046T + 0.0011T^2$ and $\varepsilon_{\mathrm{V}} = 1.006$.

Mass density:

$$\rho(T) = \rho_{\mathrm{L}}(T)[1 - H(T - T_{\mathrm{vap}})] + \rho_{\mathrm{V}} H(T - T_{\mathrm{vap}}),$$

where $\rho_{\mathrm{L}} = 1.490\,78 \times 10^{-5} T^3 - 1.788\,86 \times 10^{-2} T^2 + 6.431\,36T + 2.808\,35\,\mathrm{kg\,m^{-3}}$ and $\rho_{\mathrm{V}} = 0.6014\,\mathrm{kg\,m^{-3}}$. The third order polynomial fit for the liquid density is derived from LaLiberté and Cooper's [14] more complex empirical

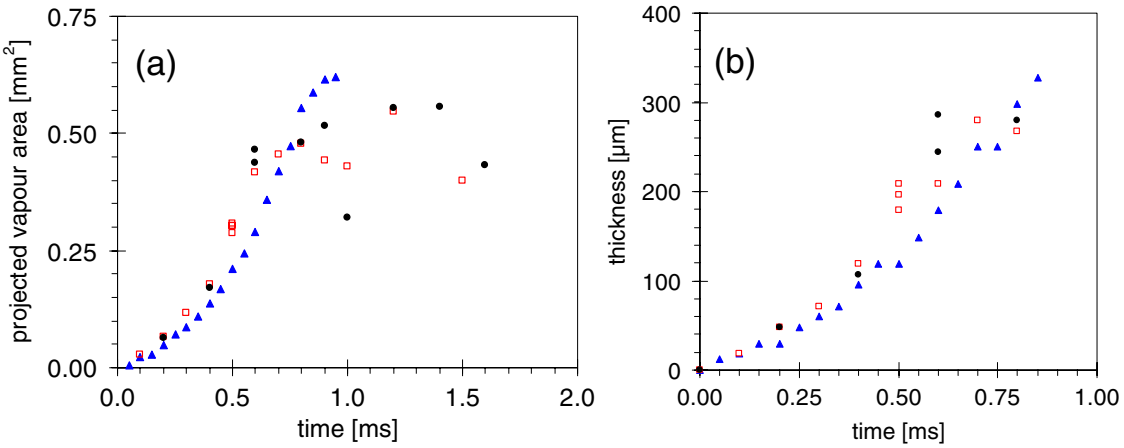

Figure 8. The time dependence of (*a*) the projected area and (*b*) thickness of the vapour layer after the start of the voltage pulse for the same conditions as in figure 2.

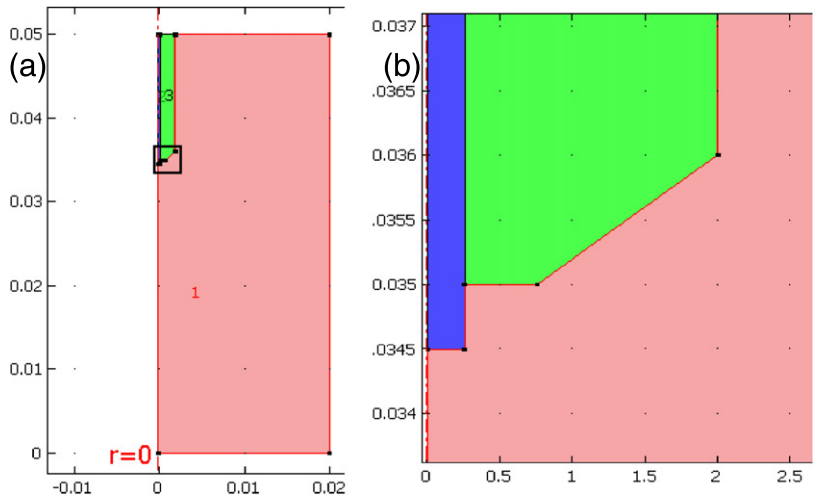

Figure 9. (*a*) The 2D-axisymmetric model geometry. (*b*) An enlarged view of the electrode tip. Colour code: the tip of the powered electrode (blue), the insulator (green) and the saline solution (pink).

equation for a 0.9% NaCl solution; it is considerably simpler and facilitates numerical computations of the density over the temperature range of interest.

Specific heat:

$$c(T) = c_{\mathrm{L}}[1 - H(T - T_{\mathrm{vap}})] + c_V H(T - T_{\mathrm{vap}}),$$

where $c_{\mathrm{L}} = 4.417\,24 \times 10^4 - 5.144\,54 \times 10^2 T + 2.306\,20 T^2 - 4.597\,34 \times 10^{-3} T^3 + 3.441\,52 \times 10^{-6} T^4\,\mathrm{J\,kg^{-1}\,K^{-1}}$ and $c_V = 2.0267\,\mathrm{kJ\,kg^{-1}}$.

Thermal conductivity:

$$k(T) = k_{\mathrm{L}}[1 - H(T - T_{\mathrm{vap}})] + k_{\mathrm{V}} H(T - T_{\mathrm{vap}}),$$

where $k_{\mathrm{L}}(T) = -0.502\,14 + 5.9679 \times 10^{-3} T - 7.5101 \times 10^{-6} T^2\,\mathrm{W\,m^{-1}\,K^{-1}}$ and $k_{\mathrm{V}} = 0.0248\,\mathrm{W\,m^{-1}\,K^{-1}}$.

3.3. Boundary conditions

Each region in the model requires appropriate boundary conditions to be specified for both the electrical and thermal response. For the electrical solution, we specify the potential V on the cylindrical tungsten electrode. Under the experimental conditions modelled there is a potential of $-200\,\mathrm{V}$ on the electrode during the vapour production phase, so this potential was also applied to the appropriate boundaries in the model (see section 2.2 and figure 2). The bottom of the cylindrical region containing the saline is held at $V = 0$, as it was in the experiment. The remaining external boundaries are specified to be electrically insulating. All other interior boundaries are allowed to be continuous, that is self-consistently determined during the simulation. For the thermal solution, we specify all external boundaries to be thermally insulating. The initial temperature is specified to be 293 K (∼20 °C). Since in this study we are just interested in short term transient phenomena, the insulating boundary condition is sufficient (it would not be appropriate for long-time steady-state solutions).

3.4. Mesh generation

The finite element method requires a geometrical mesh on which equations (2.1)–(2.4) are evaluated. COMSOL employs an automatic mesh generation routine, and enables

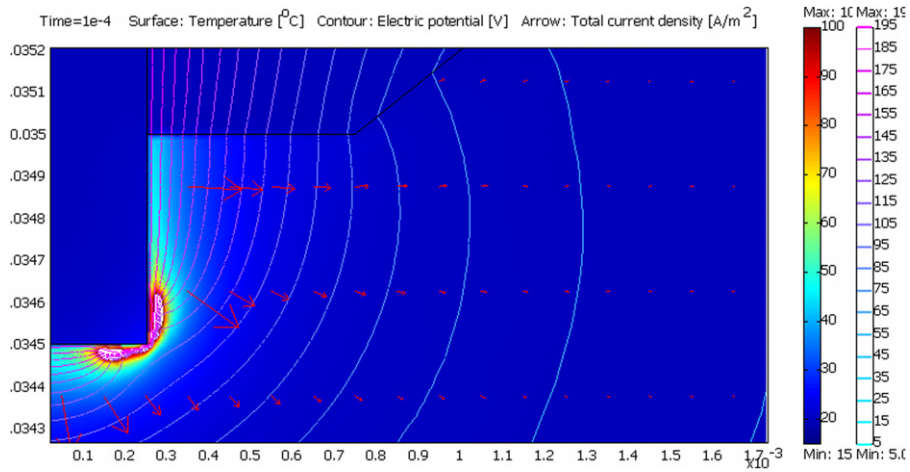

Figure 10. A 2D surface plot for temperature (colour scale at near right, white indicates temperatures above 100.15 °C, and hence vapour), contour plots for electric potential (scale at far right), and arrows for current density (relative scale length), at $t = 100\,\mu$s after initiation of a −200 V voltage pulse.

customized mesh refinement near small geometrical objects to improve resolution. Of course, higher density meshes require significantly greater time to achieve convergence and complete a given simulation. The simulations here employed about 2000 mesh elements, resulting in about 8000 degrees of freedom.

3.5. The numerical solution

Since the problem of vapour layer formation is inherently time dependent, a time-dependent transient solver algorithm was used within COMSOL. A typical simulation time was 2 ms, which is sufficient to capture the vapour layer formation dynamics for this study. The time step was 10 ns. Equations (2.1)–(2.4) are linear, so the linear system solver UMFPACK Direct linear system solver was selected, and nonsymmetric matrix symmetry was selected, which is appropriate for the equations being solved. Given the mesh parameters, the selected multiphysics couplings, the mesh described above, and the solver parameters, a typical solution took approximately 10 min to run on a PC with a 2 GHz processor and 2 GBytes of RAM.

3.6. Modelling results

Following successful completion of a particular simulation, the output data are post-processed to generate various graphs and reports. Figure 10 illustrates the data as a surface plot for temperature, contour plots for potential, and arrows for current density at 100 ms after the voltage pulse is applied. The geometry is axisymmetric, with the axis of symmetry on the left of the figure. The colour indicates temperature—red regions are hotter than blue regions.

At this time, a vapour layer (indicated in white) is seen to be growing from the high-field (and therefore high Ohmic-heating region of the saline) corner of the tungsten electrode, and is spreading laterally over the tip and along the length of the electrode. This vapour layer remains very thin, of the order of 15–25 μm thick, as it spreads over the electrode. Since the conductivity of the water vapour in the vapour layer is much smaller than that in the surrounding saline solution the equipotential lines tend to coalesce into the low-conductivity region and the electric field there is enhanced, as is well known from electrostatic theory. Since the electrostatic field is proportional to the gradient of the potential the electric field strength becomes quite large $\sim 10^7\,\mathrm{V\,m^{-1}}$; large enough to cause electrical breakdown of the vapour layer, thus causing a microplasma to be developed.

Closer inspection of these plots, as can be seen later, shows that in the transient situation modelled here there is insufficient time for the electrode to heat to temperatures sufficient to vaporize the fluid contacting the electrode. Therefore, the temperature of the fluid in contact with the electrode does not change appreciably in 1 ms. There are some other regions along the electrode surface where the vapour layer appears to be in direct contact with the metal surface, and these could be regions where electrons from the metal are field emitted into the vapour layer, thus causing breakdown of the vapour layer into a plasma.

The typical temporal behaviour of the computed electric field within a few μm from the rim of the tungsten electrode (i.e. at $r = 0.025$ m in figure 10) is shown in figure 11. The electric field increases rapidly as the vapour layer forms. The scatter in the data is reflective of the graininess of the mesh and the associated numerical noise. After approximately 0.3 ms the electric field approaches $10^7\,\mathrm{V\,m^{-1}}$, which can be sufficient to induce electron field emission from metal surfaces.

The spatial dependence of the electric field in the fully developed vapour layer on the cylindrical side of the electrode, 100 μm from the electrode rim, is illustrated in figure 12. Note that the electric field here also approaches $10^7\,\mathrm{V\,m^{-1}}$, but is somewhat reduced from that at the rim, since the curvature of metal surface is larger than at the corner.

4. Comparison between experiment and modelling: results and discussion

In figure 13 a comparison between the measured current in the experiment and the computed currents from the finite element

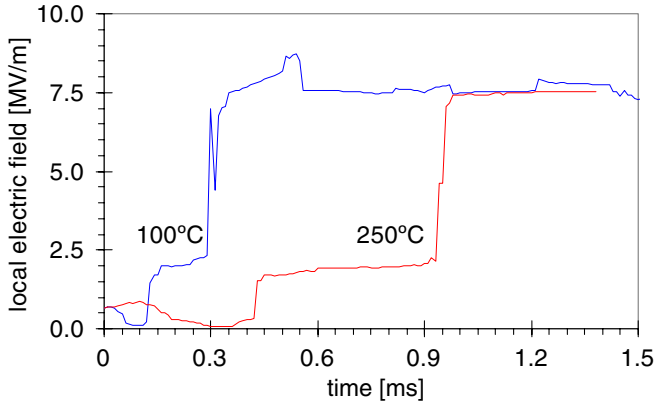

Figure 11. The computed time dependence of the electric field in the vapour layer near the corner of the tungsten electrode after initiation of a −200 V voltage pulse comparing boiling points of 100 and 250 °C.

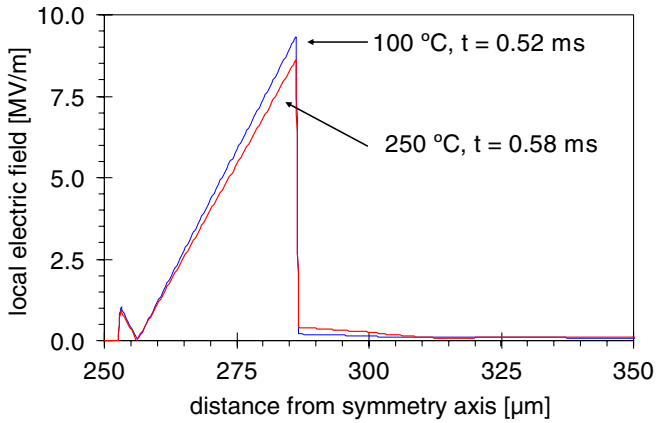

Figure 12. The spatial dependence of the electric field in the fully developed vapour layer near the electrode's cylindrical surface (at $r = 0.025$ m), 100 μm from the electrode corner.

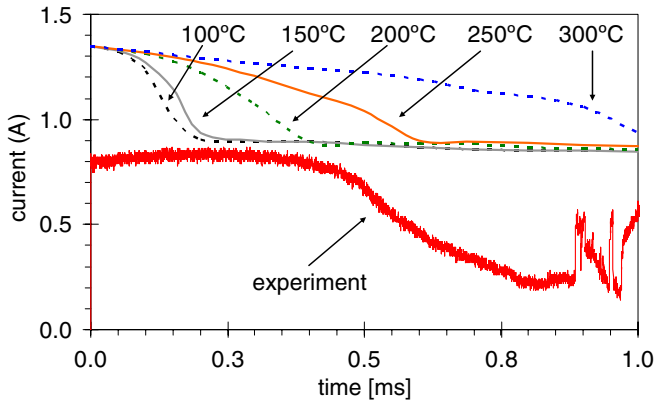

Figure 13. Comparison between experimentally measured current (red line) and the current determined from the model for various liquid boiling points.

model is presented. There are two significant observations to make. Firstly, the present model predicts currents that are about a factor of 2 larger than the measured values. However, since this is a relatively simple model containing no arbitrary scale factors and given the degree of uncertainty associated with some of the values of the physical parameters required,

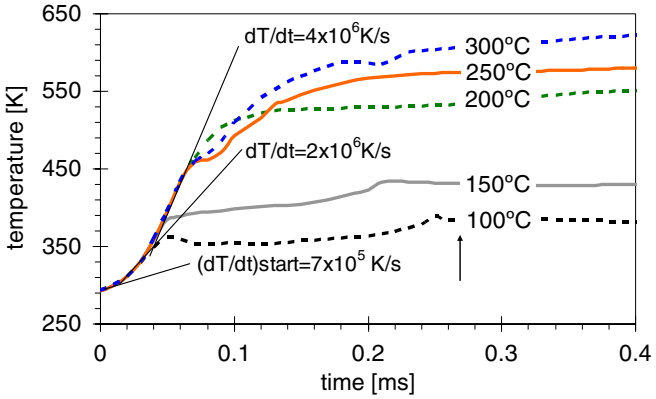

Figure 14. The computed temperature histories for various liquid boiling points. Also shown are the heating rates at various times.

we consider the agreement to be very good. Secondly, we find that the modelled current tends to decrease, due to vapour layer formation, at an earlier time than the experimental data when a boiling point of 100.15 °C for the liquid is used in the computations. We performed a parametric study to observe the effects of varying the boiling point; these results are also shown in figure 13. As can be seen better agreement for the temporal behaviour of the current is found if the boiling point is between about 250 and 300 °C.

Furthermore, we examined the temporal behaviour of the vapour layer temperature in the model near the electrode and found that there are rather rapid temperature increases, illustrated in figure 14. The behaviour of the temperature with time is similar to that seen in the vapour layer growth rate in figure 8.

Regardless of boiling point the rate of temperature increase just after the voltage pulse is applied is about 7×10^5 K s^{-1}. Depending on the boiling point selected the maximum heating rate may be as large as 4×10^6 K s^{-1}. It is known from other work that liquids subjected to such fast heating rates may be able to be superheated above their boiling point for short times before sudden vaporization begins. For example, Glod *et al* [18] studied microscale explosive vaporization of water heated by a resistively heated thin platinum wire and found that they could achieve explosive vaporization at the spinodal limit of about 303 °C with heating rates between about 10×10^6 and 86×10^6 K s^{-1}. The heating rates in that work were larger by at least a factor of 2 compared with what our model shows. However we note that Glod *et al* believe that their experiment is governed by heterogeneous nucleation (on the wire surface) of boiling at the lower heating rates they employed, and homogeneous nucleation (in the bulk fluid) at the higher heating rates.

Our model, as well as the experiment, is studying a somewhat different system where the saline is heated resistively in the bulk of the fluid rather than by conductive heating from a bare wire. So we believe our experiment and model should be governed by homogeneous nucleation of vaporization in bulk of the saline. Indeed our simplified model shows that a thin liquid layer tends to stick to the electrode, further supporting our view that the vaporization is a homogeneous process.

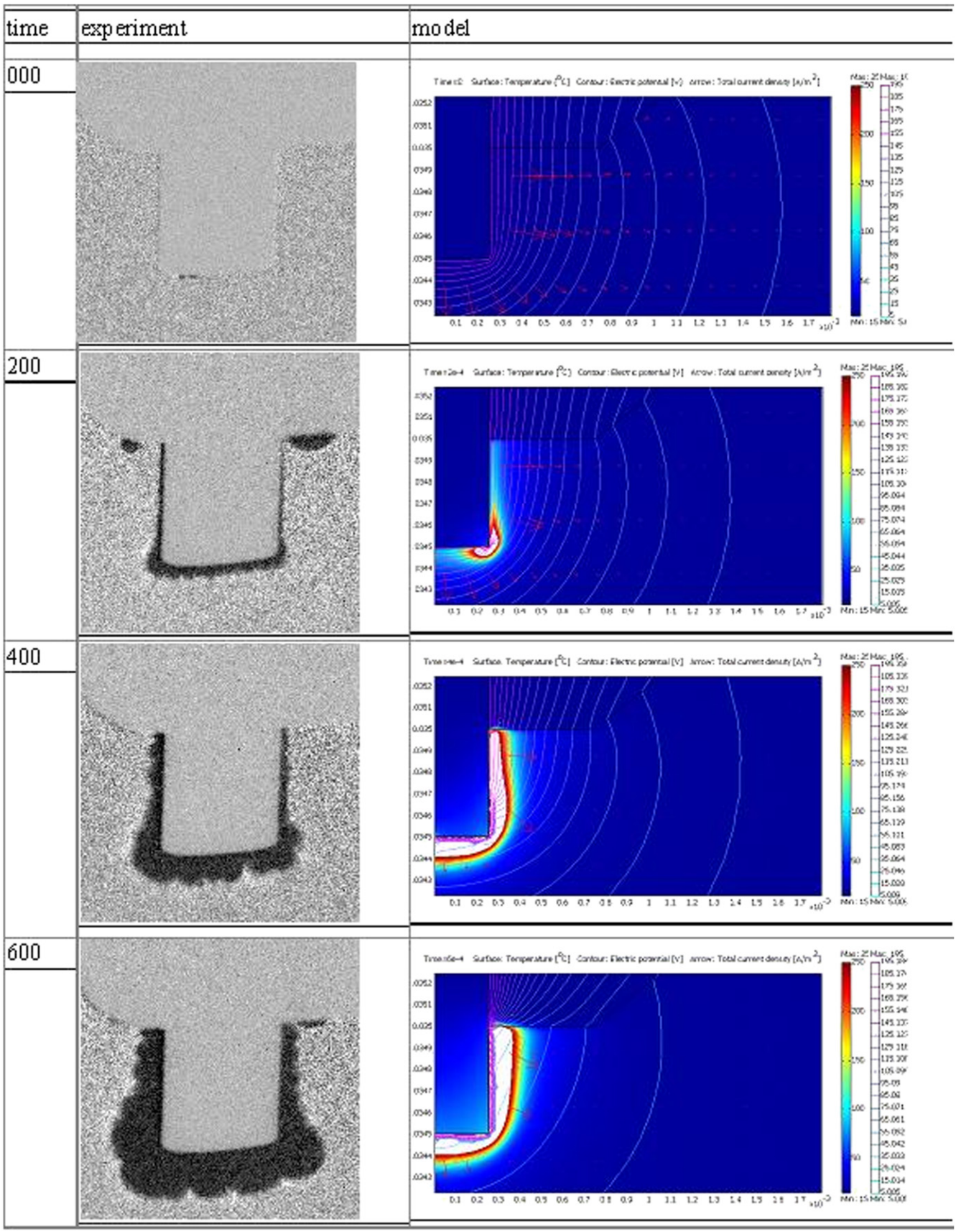

Figure 15. A side-by-side comparison between the experimentally observed vapour layer production and the model results.

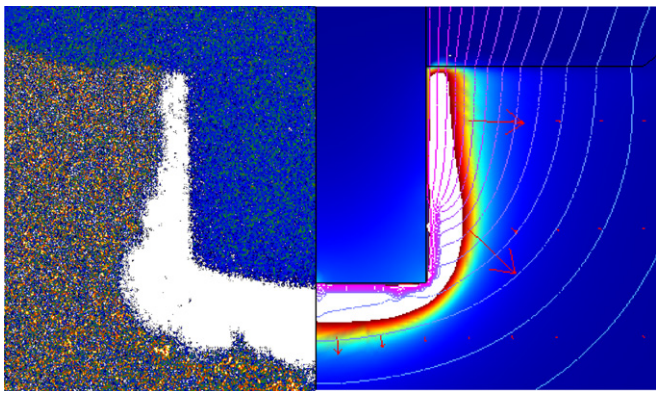

Figure 16. An overlay of measured (left) and calculated (right) vapour layer for a −225 V pulse at 400 μs into the pulse.

In figure 15 we present a side-by-side comparison of shadowgraphs from the experiment with the model results at 200 μs intervals. The shadowgraph is scaled to the model using the common size of the electrode tip. The experiment shows that the vapour layer tends to start forming rapidly over the entire flat tip end, with perhaps thicker vapour layer formation at the rim of the electrode, and then spreads laterally and lengthwise along the curved part of the electrode. The model consistently shows that the vapour layer begins to form at the rim of the tungsten electrode and expands laterally along the flat tip end as well as along the curved part of the electrode towards the insulator. Both model and experiment show that the vapour layer completely covers the entire electrode after about 400 μs. We believe the model is reflecting the much larger Ohmic heating at the high-field corner region. We do not at present understand why the experiment shows more uniform initial vapour layer production on the flat tip of the electrode.

In figure 16 two images, one from the experimental shadowgraph and the other from a simulation, are shown. Again the results compare very well. At the time of this comparison the experiment shows complete coverage while in the model it is not quite at completion. Overall the layer in the model is somewhat thinner than that observed experimentally.

Hence, with the simplified multiphysics coupling employed in this work we find reasonably good agreement between experiment and the model, but we do observe some differences as well. We expect that as we incorporate more physics (for example, surface tension, and mass, momentum and energy conservation, as well as latent heat of vaporization), the model and experimental results will converge to even better agreement.

In addition to incorporating more physics into the model, we will also be employing more advanced numerical modelling methods to more robustly deal with phase changes that dominate the physics. Many problems involving phase changes, and other significant changes in physical parameters as a result of the phase changes, are difficult to solve using finite element methods due to the stiffness of the problem's equations. Several numerical methods have been developed to deal with phase changing phenomena, including front-tracking [19] and level set methods [20]. We found in this initial study that we could achieve very good convergence and reasonable computation times without employing these advanced methods. Since our initial, simplified analysis presented here does not conserve mass, momentum and energy, nor take into account surface tension of the fluid, as is done with the more advanced methods, our solutions lack some details. Nevertheless, the simplicity of our model does lead to results which are in very good agreement with the experimental results, and it does elucidate some fundamental features of the vaporization process.

5. Conclusions

In conclusion, we have compared optical measurements of the dynamical evolution of a vapour layer forming around an electrode immersed in a saline liquid and subjected to a low (∼200 V) voltage pulse. A simplified finite element multiphysics simulation of the system, including Ohmic heating, heat conduction and electrostatics, reproduces much of the observed behaviour. The simulations suggest that rapid superheating of the saline near the electrode results in vaporization occurring well above the normal boiling point of the solution, approaching the non-equilibrium spinodal limit. The simulations also show that the electric field strength in the low-conductivity vapour layer near the electrode increases significantly over its value prior to the onset of vaporization, and combined with the reduced vapour density produces E/N values sufficient to breakdown the vapour and form a non-equilibrium microplasma. These discharge phenomena are discussed in a companion paper [7].

Acknowledgment

Lucas Schaper was supported by a European Union Social Fund Postgraduate Studentship.

References

[1] Stalder K R and Woloszko J 2007 Some physics and chemistry of electrosurgical plasmas *Contrib. Plasma Phys.* **47** 64–71
[2] Sengupta S K, Srivastava A K and Singh R 1997 Contact glow discharge electrolysis: a study of its origin in the light of the theory of the hydrodynamic instabilities in local solvent vapourization by Joule heating during electrolysis *J. Electroanal. Chem.* **427** 23–7
[3] Kobayashi K, Tomita Y and Sanmyo M 2000 Electrochemical generation of hot plasma by pulsed discharge in an electrolyte *J. Phys. Chem.* B **104** 6318–26
[4] Wetz D A Jr, Mankowski J J, Dickens J C and Kristiansen M 2006 The impact of field enhancements and charge injection on the pulsed breakdown strength of water *IEEE Trans. Plasma Sci.* **34** 1670–9
[5] Woloszko J, Stalder K R and Brown I G 2002 Plasma characteristics of repetitively-pulsed electrical discharges in saline solutions used for surgical procedures *IEEE Trans. Plasma Sci.* **30** 1376–83
[6] Stalder K R, Nersisyan G and Graham W G 2006 Spatial and temporal variation of repetitive plasma discharges in saline solutions *J. Phys. D: Appl. Phys.* **39** 3457–60
[7] Schaper L, Stalder K R and Graham W G 2011 *Plasma Sources Sci. Technol.* **20** 034004

[8] Lykelma J 1995 *Fundamentals of Interface and Colloid Science* vol 2 (New York: Academic)
[9] COMSOL Multiphysics 2005 Version 3.2, COMSOL AB, Stockholm, Sweden, © 2005
[10] Stogryn A 1971 Equations for calculating the dielectric constant for saline water *Trans. Microw. Theory Tech.* **19** 733–6
[11] Colin E, Clarke W and Glew D N 1985 Evaluation of the thermodynamic functions for aqueous sodium chloride from equilibrium and calorimetric measurements below 154 °C *J. Phys. Chem. Ref. Data* **14** 489–610
[12] Carlson H R April 1980 *Electrical Conductivity And Infrared Radiometry Of Steam, ARCSL-SP-80006* US Army Armament Research and Development Command, Chemical Systems Laboratory, Aberdeen Proving Ground, MD 21010
[13] Fernandez D P, Goodwin A R H ,Lemmon E W, Levelt J M K, Sengers J V and Williams R C 1997 A formulation fo the static permittivity of water and steam at temperatures from 238 K to 873 K at pressures up to 1200 MPa, including derivative and Debye–Hückel coefficients *J. Phys. Chem. Ref. Data* **26** 1125–66
[14] LaLiberté M and Cooper W E 2004 Model for calculating the density of aqueous electrolyte solutions *J. Chem. Eng. Data* **49** 1141–51
[15] Weast R C (ed) 1977 *CRC Handbook of Chemistry and Physics* 58th edn (Cleveland, OH; CRC Press)
[16] Ozbek H and Phillips S L 1980 Thermal conductivity of aqueous NaCl solutions from 20 C to 330 C *J. Chem. Eng. Data* **25** 263–7
[17] Sengers J V, Watson J T R, Basu R S, Kamgar-Parsi B and Hendricks R C 1984 Representative equations for the thermal conductivity of water substance *J. Phys. Chem. Ref. Data* **13** 893–933
[18] Glod S, Poulikakos D, Zhao Z and Yadigaroglu G 2002 An investigation of microscale explosive vaporization of water on an ultrathin Pt wire *Int. J. Heat Mass Transfer* **45** 367–79
[19] Trygvasson G, Bunner B, Esmaeeli B A, Juric D, Al-Rawahi N, Tauber W, Han J, Nas S and Jan Y-J 2001 A front-tracking method for the computations of multiphase flow *J. Comput. Phys.* **169** 708–59
[20] Sethian J A and Smerka P 2003 Level set methods for fluid interfaces *Ann. Rev. Fluid Mech.* **35** 341–72